Salinas-Farran *et al. Biochar* (2024) 6:86
https://doi.org/10.1007/s42773-024-00374-7

Biochar

ORIGINAL RESEARCH Open Access

Tracked evolution of single biochar particle's morphology during pyrolysis in *operando* x-ray micro-computed tomography

Luis Salinas-Farran[1,2†], Maryanne Chelang'At Mosonik[1†], Rhodri Jervis[3], Shashidhara Marathe[4], Christoph Rau[4] and Roberto Volpe[1*]

Abstract

The engineering of biochars with desired morphologies and pore structures is a far-reaching objective towards sustainable pore-dependent environmental technologies, such as water and soil remediation or catalysis. We hereby report a series of experiments that allow the direct following of the shape and porosity of single biochar particles during pyrolysis. Particles ~ 1–2 mm in diameter of unwashed and water-washed raw walnut shells were continuously 3D imaged during pyrolysis to 575 ℃ at a 10 K min^{-1} in Ar to obtain time- and temperature-resolved x-ray micro computed tomographies to a 0.82 µm resolution. Results showed visual evidence of a 30% and 70% v/v particle shrinkage for unwashed and washed samples, respectively. Particle swelling between 200 and 300 ℃ in the unwashed sample provided evidence of the softening of native biopolymers associated with lignin in untreated biomass. A purpose-defined parameter Λ shows the temperature-dependence of pore re-distribution towards the center of the particle to be linear for both samples. Λ was found to be $3.2 \times 10^{-4} K^{-1}$ in the washed sample, approximately 3.5 times faster than in the unwashed one. Such linear dependence is significantly slower than an exponential Arrhenius-like trend thereby providing a qualitative measure of the heat and mass transport phenomena limiting the chemical reactions in the porous medium. This evidence is key to resolving the pathways to the thermochemical decomposition of biomass leading to preparation of precision-engineered biochars.

Highlights

- Evolution of morphology of single particle (1–2 mm) walnut shell was tracked *in operando* during pyrolysis via micro-CT (~ 812 nm resolution).
- Samples pre-washed in water didn't exhibit particle swelling observed in untreated samples in the 200–300 ℃ range.
- Porosity towards the center of the particle was developed 3.5 faster in washed samples than in unwashed ones.

Keywords Pyrolysis, Biochar, *Operando* Imaging, Tomography

† Luis Salinas-Farran and Maryanne Chelang'At Mosonik co-first authors.

*Correspondence:
Roberto Volpe
r.volpe@qmul.ac.uk
Full list of author information is available at the end of the article

Graphical Abstract

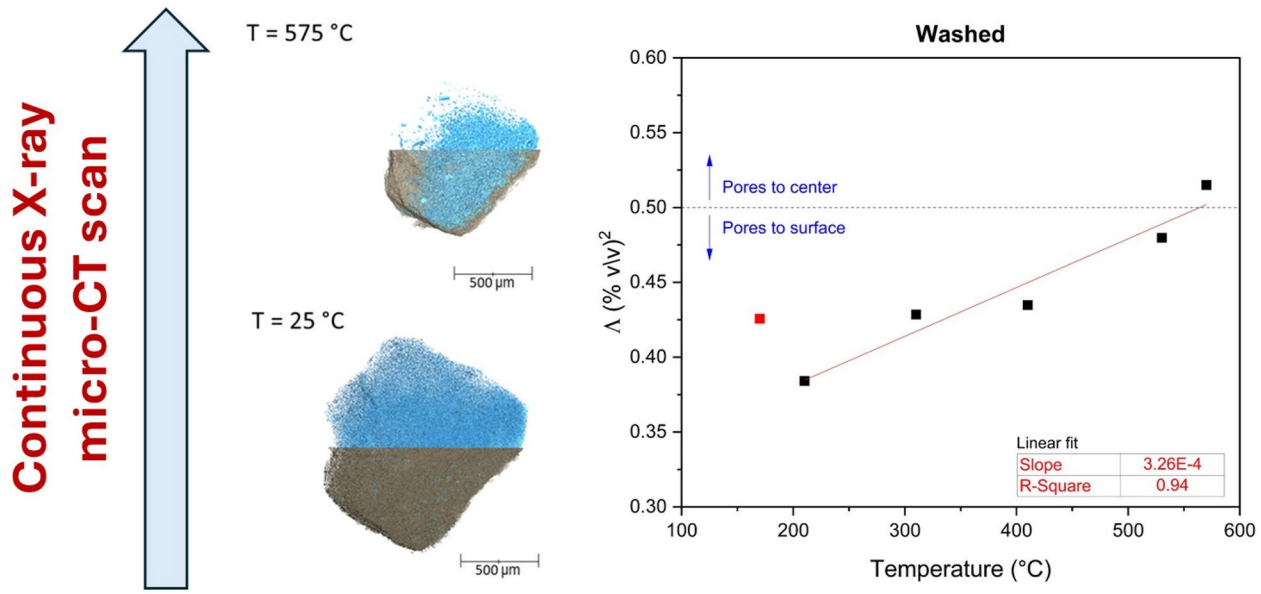

1 Introduction

Biochar is the solid, porous, carbonaceous product of biomass pyrolysis (Liu et al. 2015). Among biomass types, agricultural wastes, such as olive stones, almonds and walnut shells (WSs) are examples of feedstocks that may be used for the production of biochar (Di Blasi 1997). In recent years, there has been a sharp rise in the interest in biochars. Their porous nature and native surface functionality make biochar attractive for several pore-dependent energy and environmental applications such as capturing and storing CO_2 to help mitigate climate change (Lorenz and Lal 2014; Shafawi et al. 2021; Singh et al. 2022), removing chemical or biological pollutants from contaminated water(Mohanty et al. 2014; Mohanty and Boehm 2015; Krasucka et al. 2021; Li et al. 2022) or providing a stable and environmentally sustainable support for catalytic applications (Guo et al. 2022; Younis and Kim 2022; Li et al. 2023; Yang et al. 2023).

What makes biochar a particularly attractive material is the possibility to tune its morphology and chemistry via simple thermal processes. Reactor design, sample size and configuration, peak temperature, heating rate (HR), holding time (HT) at peak temperature (PT), sweep gas type and velocity are the main operation parameters that can be varied to influence the resulting biochar morphology (Di Blasi 1997). However, in addition to these controllable parameters, morphology greatly depends on the type of feedstock and its diverse, largely inhomogeneous biopolymeric composition as well as the presence in its matrix of different quantities of inorganic elements, typically belonging to the alkaline and alkaline hearth metal groups. Broadly, feedstocks with higher contents of three-dimensional cross-linked biopolymers, attributed to lignin (which in the following we will refer to as 'lignin'), have been found to yield higher quantities of biochars that are typically more thermally stable (Rodriguez Correa et al. 2019), with a significant role played by the inorganic compounds. We have chosen WS because of its higher content in lignin as reported in (Chelang'At Mosonik et al. 2021). Combined, this diversity and the aforementioned reaction parameters allow for a virtually infinite combinations of biochar characteristics, such as morphology, porosity, surface pH and polarity (Uday et al. 2022). Microporosity, adsorption capacity, ion exchange capacity, and electrical conductivity are some of the desired characteristics for the aforementioned applications: water remediation, carbon sequestration and catalysis (Uday et al. 2022; Tagar et al. 2023).

Extensive experimental and computational modelling efforts have been undertaken in the attempt to correlate sample type and configuration and preparation conditions to resulting particle structures and compositions. Yet the changes in feedstock textural and chemical properties during pyrolysis are the result of numerous, largely unresolved chemical reactions occurring in the confined space of an evolving reactive medium both in the

homogeneous (gas–gas, vapor-vapor, solid–solid) and heterogeneous (gas–vapor-solid) environments (Antal and Grønli 2003; Morgan and Kandiyoti 2014; Kandiyoti et al. 2017). Advanced modelling carried out by Ghoniem's group at Massachusetts Institute of Technology (Singer and Ghoniem 2011, 2013; Bates and Ghoniem 2012; Bates et al. 2016), and experiments carried out by Kandiyoti's group at Imperial College London, (Stiles and Kandiyoti 1989; Morgan and Kandiyoti 2014; Kandiyoti et al. 2017) among several others have greatly contributed to elucidation of part of the aforementioned complexities in different set-ups. Janse and coworkers (Janse et al. 2000) investigated the influence of particle morphology in flash pyrolysis by simulating cylindrical, spherical and flat particle shapes. The spherical particle showed fastest conversion; however, the influence of shape became insignificant once small particle diameters of less than 200 μm were converted. Computational Fluid Dynamics (CFD) has been used extensively to model a large number of existing pyrolysis reactors (Dadi et al. 2023); however, simulations are often based on specific particle geometries (spherical, cylindrical pellet, etc.) (Hu et al. 2020). Although necessary to reduce computational burden, such assumptions greatly limit the validity of the results. Biomass particles are always morphologically irregular and exhibit a wide variety of geometries of their pore networks at all of the supra- and infra-micrometric and nanometric scales. These complex porosities cause heat and mass transport limitations that affect the nature and kinetics of the chemical reactions, and, in turn, the process outcomes. Recent models of the reactions at the molecular level using quantum chemistry and other techniques at the multiscale level (Ciesielski et al. 2020) provide potentially interesting clues as to some of the reaction pathways. Yet these models, especially those at the quantum scale, require clearly determined and uniform molecular compositions of biomass (hemicellulose, cellulose, lignin) and assume that thermal behaviors of such simulated molecular constituents are additive.

We have proved that this theoretical assumption, although certainly useful to progress fundamental understanding, is not valid in real experimental set-ups where synergistic effects among biomass macroconstituents during thermal decomposition are non-negligible (Barr et al. 2021; Volpe et al. 2018). In addition, owing to the necessary small scale, key to controlling computational complexity, the effects of extra particle reactions which again appreciably influence process outcomes, even at the milligram sample sizes are often neglected (Barr et al. 2020). The pyrolysis of single particles, of different nature, sizes and shapes to different thermal regimes and atmospheres has been studied by several authors for decades in different works that we have recently commented on in more detail (Barr et al. 2021). We complemented those works with a set of *operando* x-ray radiography of pyrolysing beds of biomass (WS and almond shells 1–2 mm particle size in a 3 mm internal diameter quartz tube, 6 mm bed height), coupled with x-ray micro computed tomography (CT) of the obtained biochars (Barr et al. 2021). Our work provided evidence that, in that set-up, (1) external and internal solid volume loss (bulk particle shrinkage and porosity gain) occur simultaneously, (2) pyrolysis leads to a redistribution of pore volume away from particle surfaces, (3) almond shell particles experience greater changes in bulk volume and smaller changes in pore volume compared to WS particles, despite their similar composition, owing to the more porous nature of the raw almond shell, which facilitates heat and mass transport when compared to less porous WS. We also proved that an alkaline pretreatment of raw biomass reduced those differences. Importantly, in our work we discussed the challenges and limitations of existing models that attempt at studying and predicting the pathways to volume loss of particles via pore opening and particle shrinkage and provided initial evidence of pore opening throughout the particle volume, yet we recognized that only an *in-situ* tracking of the evolution of particle morphology and porosity can provide necessary evidence on the exact localization of pores opening during the process. Such evidence was missing.

In the present work, we further advanced our findings through a novel set of *operando* x-ray micro-CT of single pyrolyzing biomass particles. Understanding the evolution of the microstructure of biomass has remained "one of the top ten challenges in biomass pyrolysis" (Mettler et al. 2012) and is necessary to contributing to the understanding of biomass pyrolysis (Antal and Grønli 2003). To our knowledge, an *in-situ* observation of the internal change in morphology of single biochar particles using micro-CT has never been presented before. Our experiments allowed a quantified analysis of the morphological evolution (particle size and porosity) of single pyrolyzing raw and H_2O pre-washed WS. It is important to note that, as described in Barr et al. (2019), the results discussed in the present manuscript are specific to the sample type and configuration that normally shows significant intrinsic variability from one experiment to the other in biomass pyrolysis. As such, the present results aim at discussing some general trends and providing insights in the fundaments of pyrolysis of WS as well as an initial indication for the engineering of biochars with tuned morphologies.

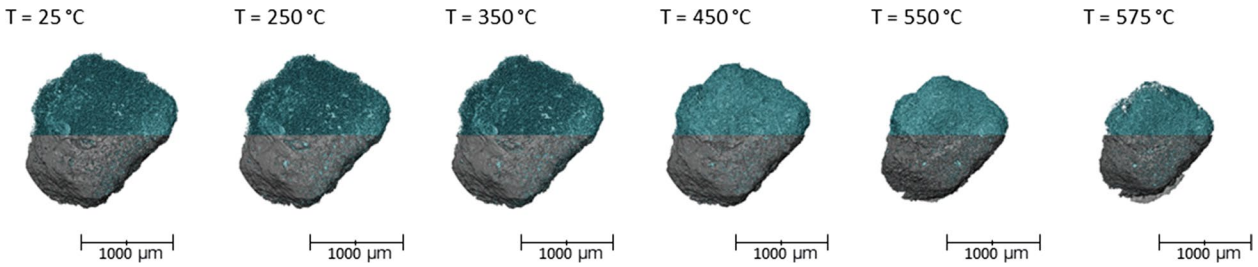

Fig. 1 3D rendering of the x-ray micro computed tomography obtained for a single unwashed particle of walnut shell at different temperatures over thermal treatment at ~ 12.5 K min^{-1} heating rate, from 25 ℃ to 575 ℃ peak temperature and 10 min holding time, in 10 L min^{-1} of Ar. Volume of solid is represented in grey color, volume of pores in light blue color

2 Results

2.1 Change in the particle volume

Obtaining a series of 3-dimensional x-ray CT tomograms throughout the pyrolysis process of the single particles of biomass allows for *operando* tracking of the change in morphological properties of the material. Approximately 260,000 images were analysed and segmented to allow tracking of both volume and pore structure up to ~ 575 ℃ temperature in an Ar atmosphere.

A 3D rendering or particles shown in Fig. 1 provides a visual representation of the significant variation in both the volume of particle and pores geometry occurring during the thermal treatment.

Figure 2 represents the same 3D rendering of the thermally treated particle and segmented (binarized) images in 2D sections in three orthogonal planes.

The total volume of single particles and voids (pores) obtained from CT data was measured at each time step and results are plotted in Fig. 3.

Results confirm a particle shrinkage with thermal treatments, recently modelled by Cho and Kong (Cho and Kong 2023) and previously modelled by Di Blasi and co-workers (Di Blasi 2008) among others. As mentioned this was also reported by the present authors for the pyrolysis of packed beds of the same size WS particles at 6 ℃ min^{-1} HT in a 3 L min^{-1} of Ar (Barr et al. 2021). Here we observe a ~ 30% and ~ 70% v/v volume loss for the unwashed and washed samples, respectively. This significant difference is attributed to the thermal robustness of aromatics present in lignin and their relation with alkali metals which are expected to be present in larger proportion in the unwashed *vs*. the washed sample (Deng et al. 2020).

Importantly, the unwashed sample shows an appreciable increase in volume in the 200–300 ℃ range, probably also linked to the softening and swelling of lignin at lower temperatures, reported already in the early 1990's by Ericksson and coworkers (Eriksson et al. 1991), among others. Accordingly, this increase in volume is not present in the washed sample. The softening of the lignin fraction more pronounced when less amount of alkali metals is present is also probably responsible for the sudden drop of the particle volume occurring at just over 300 ℃, a 'turning-point' temperature reported by Volpe and coworkers using different techniques in previous works (Volpe et al. 2015, 2016, 2019b). As such, the expected lower content of alkali metals in the washed sample causes a delay in the onset of particle shrinkage to approximately 450 ℃; however, a much more pronounced volume loss at the higher temperatures is observed.

The similarity in the shapes of the plot between the overall particle and particle material volume changes, (grey and blue, respectively in Fig. 3) is a clear indication that up to 450–500 ℃ the loss in particle volume is significantly linked to the devolatilization of the solid matrix, while for temperatures above those values, the opening of pores becomes also more significant.

2.2 Evolution of porosity

The total volume of pores and the total volume of particle material (including pores) was tracked through the pyrolysis process and the overall porosity at a given temperature was calculated using Eq. (1):

$$\phi_T = \frac{V_{pore,T}}{V_{material,T} + V_{pore,T}} \tag{1}$$

where ϕ_T is the overall porosity (or pore volume per unit particle volume), $V_{pore,T}$ is the total volume of pores at temperature T, and $V_{material,T}$ is the volume of the particle solid material (not including pores) at the same temperature. We indicate with $\phi_{initial}$ the initial value of ϕ_T.

Values of ϕ_T and $\frac{\phi_T}{\phi_{initial}}$ plotted *vs.* temperature can be found in.

Washed WS shows a higher percentage of pores compared to the unwashed sample: an average 10% higher ϕ_T is maintained on the washed sample throughout all the process. The initial higher porosity of the washed sample is caused by water dissolving organic acids (associated

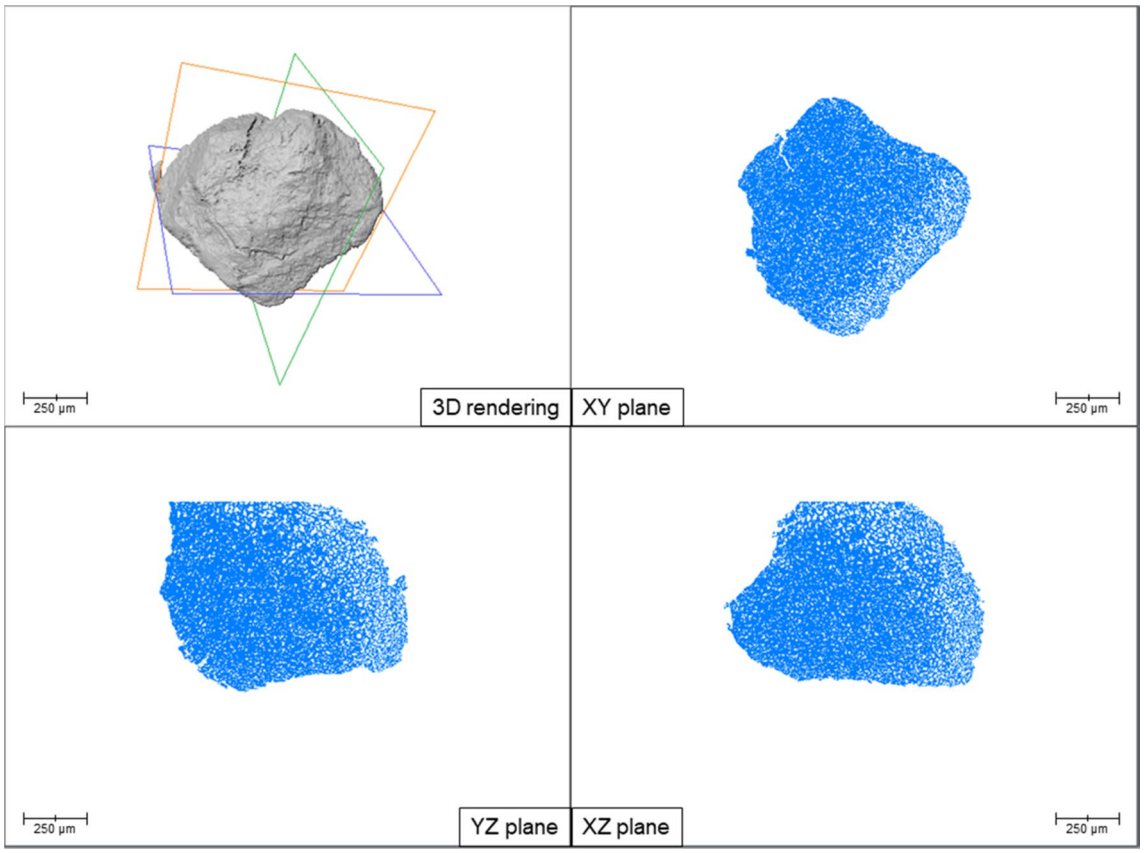

Fig. 2 3D rendering of single particle of walnut shell thermally treated at ~ 12.5 K min^{-1} heating rate, to 575 ℃ peak temperature and 10 min holding time, in ~ 10 L min^{-1} of Ar, and 3 2D segmented images. Light blue represents solid portion, white represents a void

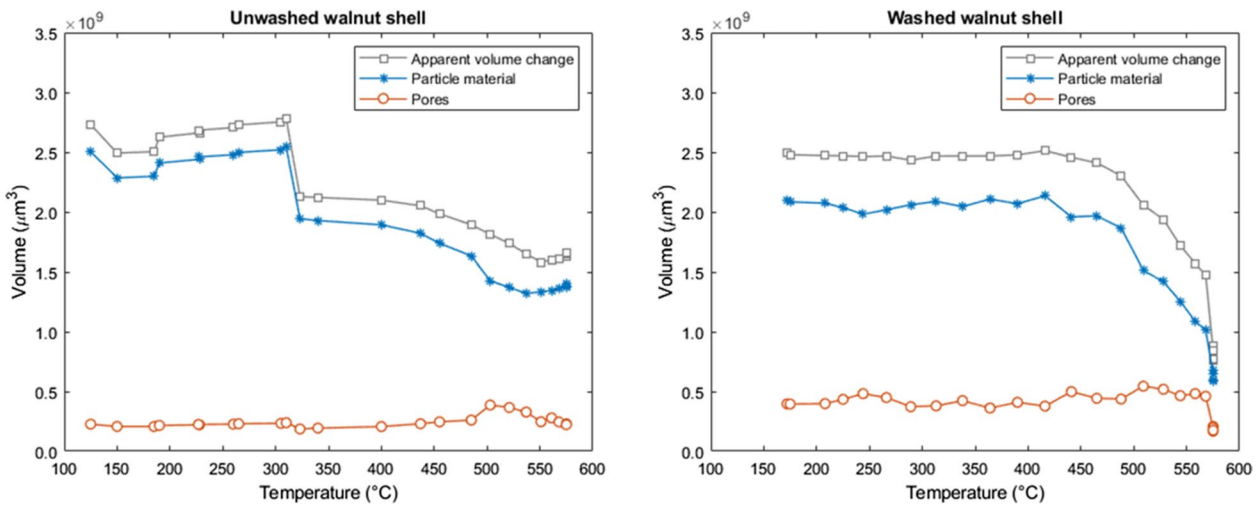

Fig. 3 Total particle volume (inclusive of pores, □ grey), particle volume (✳ blue) and pore volume (○ red) plotted *vs.* temperature during biomass pyrolysis at ~ 12.5 K min^{-1} heating rate in 10 L min^{-1} of Ar. Each data point represents analysis from a 3D x-ray CT data set, taken sequentially throughout the pyrolysis process

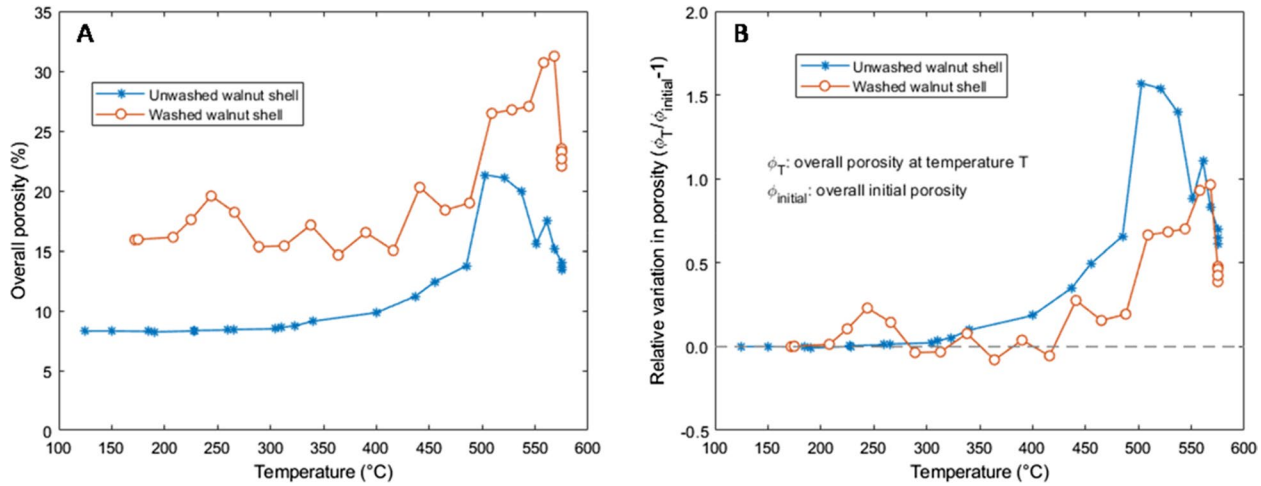

Fig. 4 Porosity changes as a function of temperature. **A** Overall changes in particle porosity as a percentage of the total particle volume (ϕ_T); **B** The changes in particle porosity relative to the initial porosity ($\frac{\phi_T}{\phi_{initial}} - 1$)

with hemicellulose), and other water-soluble organic compounds present in the raw biomass including aromatics related to lignin such as toluene and styrene (Deng et al. 2020).Water washing is also well known to leach inorganics present in the biomass (Taylor et al. 2020; Lee et al. 2020). The solubilization of some organic compounds and leaching of inorganics are responsible for the opening of pores that facilitate heat and mass transport during pyrolysis, thereby facilitating the development of higher porosity. This evidence provides important indication for the use of mild pretreatments (such as water washing) to improve porosity in biochars.

The broad trends in the development of porosity in both samples are similar; however, the following notable elements emerge (Fig. 4B):

1) Both samples show a marginal or negligible increase of porosity during a generally steady pores development regime, to a certain temperature, from which porosity starts to increase. This temperature was shown to be ~ 320 ℃ for the unwashed samples and ~ 420 ℃ for the washed sample. The 320 ℃ "turning point" has been reported by Volpe and coworkers in previous works where the change in the pyrolysis evolution regime was related to a release of hydrogen above the 300–330 ℃ temperature mark in similar set-ups using different analytical techniques (Volpe et al. 2015, 2016, 2019a). Notably, during the generally steady pores development regime, the porosity of the washed sample showed more variability (~ 5%) with temperature. We attribute this to the fraction of organic and inorganic compounds dissolved by the washing and the less 'stable' solid matrix resulting from it. It is important to also consider that the washing procedure introduces some uneven changes on the surface of the samples due to water permeating the inner pore network of biomass in an uneven way depending on a combination between pore size (larger pores are washed more easily and more effectively than smaller ones, due to water surface tension) and surface functionalities (Barr et al. 2022).
2) Porosity increases sharply from ~ 470 ℃ to approximately 500–550 ℃, then sharply decreases and remains stable during holding at PT. These sharp changes are largely affected by the reductions in the overall particle volumes which appears at the denominator in ϕ_T as shown in Fig. 3 where the pore and particle volumes appear to diverge significantly (pores increase, volumes decrease) between the aforementioned regime changes points (320 ℃ for the unwashed sample and 420 ℃ for the washed one) and 500–550 ℃.

2.3 Redistribution of porosity inside the particle

The changes of temperature are also responsible for a redistribution of the porosity inside the particle. In this section we attempt at a calculation of that redistribution and its dependence on temperature.

If we consider the particle to be a sphere of radius R, then the mean porosity for the particle can be calculated by the following expression:

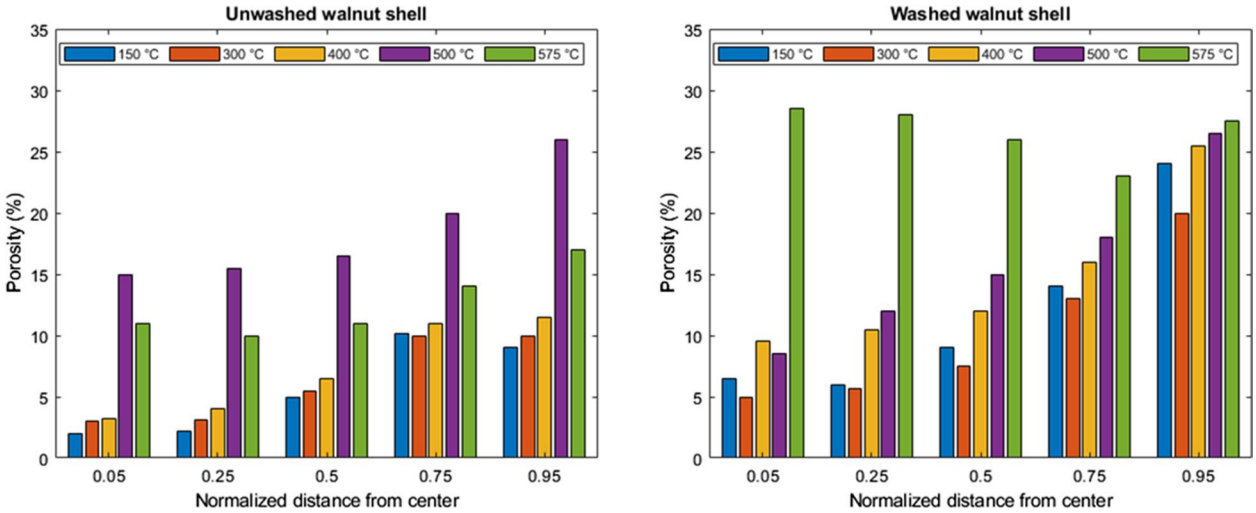

Fig. 5 Distribution of porosity inside the particles. Porosity is calculated as defined in Eq. 1 for volumetric shells positioned at a distance from particle surface indicated as a normalized value in the *x* axes of the diagrams

$$mean\,porosity = \frac{\int_0^R f(r)\frac{4}{3}\pi r^2 dr}{V_{material} + V_{pore}} \tag{2}$$

which can be approximated by:

$$mean\,porosity \approx \frac{\sum_{i=0}^{n-1} f(r_i)\frac{4}{3}\pi r_i^2 (r_{i+1} - r_i)}{V_{material} + V_{pore}} \tag{3}$$

where $f(r)$ is the porosity function, which varies with radius and represents the porosity ϕ_T at a given distance from the center (i.e. the porosity of a given volumetric shell comprised between radii r_{i+1} and r_i), where i is equally spaced out at a 1 pixel distance (or 825 µm), and $r_n = R$.

This simplification is particularly useful to track the changes in porosity with radius and therefore to identify the changes in location of pores with temperature simply by changing the intervals of integration or sum in Eqs. (2) or (3) respectively. At each radius the total volume at denominators in Eqs. (2) and (3) is calculated as the volume of the sphere at that radius.

Values at specific distances from the particle center are plotted *vs.* temperature in Fig. 5, where distance from center has been normalized to values comprised to 0 (the center) and 1 (the surface) to provide a direct comparison among solid particles of changing volumes.

For each of the two samples, porosity evolves consistently in all the particle's volumetric shells. Thus, in both the samples all shells broadly follow the overall particle behavior reported in Fig. 4, i.e. porosity in the unwashed samples peaks at 500 ℃ and then decreases, while it continuously increases with temperature in the washed one. However, the redistribution of pores (i.e. the increase in porosity) towards the center of the particle becomes significant in the washed sample at 575 ℃. At that temperature the washed sample has reached a broadly uniform distribution of pores across the volume. This is a particularly relevant indication of the effect of pre-washing feedstock if a pore-dependent application is sought, where accessing pores located towards the center is expected to increase surface contact with the medium.

In addition, these results indicate that the core of the particle is more susceptible to thermal decomposition for temperatures higher than 550 ℃ when samples are pre-washed. This can also be seen as an effect of the higher degree of thermal stabilization in the unwashed sample, which, as discussed, is richer in inorganics, responsible for faster graphitization via nucleation of graphitic domains (Malik et al. 2023). These findings also corroborate what Klose and Schinkel (Klose and Schinkel 2002) have predicted through their model regarding the coalescing of smaller pores with temperature.

The total volume of pores in each shell can be divided by the total volume of pores in each particle at each temperature (i.e. at each CT scan) in a way that the cumulative porosity from the shell or radius 0 (at the center) to that of radius R (at the surface) will be equal to the total volume of pores in the sphere representing the particle. These values can be normalized to be comprised between 0 (0 porosity at the center of the particle) and 1 (total pore volume at radius R) to obtain a direct comparison between particles at different temperatures. Figure 6 reports a generic representation of such normalization plotted *vs.* normalized shell volumes.

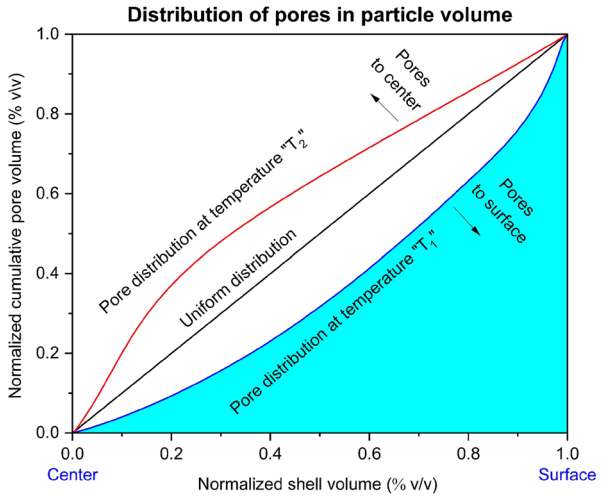

Fig. 6 Representation of cumulative pore volume (normalized with respect to the total volume of pores in the particle) *vs.* shell volume (normalized with respect to total particle volume) at generic temperatures T_1 (blue) and T_2 (red). The straight black line represents a theoretical uniform distribution of pores across the particle volume. The area colored in light blue represents the value of Λ at temperature "T_1" as defined in Eq. (4)

In such plot an equally distributed porosity through the particle is represented as a straight line with slope 1, indicated as 'uniform distribution' in the figure. The more the curves in Fig. 6 'deflect' from that straight line, the more the porosity is concentrated towards the center (convex curves) or the surface (concave curves). A measure of that 'deflection', given by the integral below each curve, is therefore useful to define the degree of pore concentration "Λ", as the following equation:

$$\Lambda = \int_0^1 P(\upsilon) d\upsilon \tag{4}$$

where $P(\upsilon)$ is the function of the porosity P with respect to υ, the volume fraction of each shell with respect to total particle volume.

Given its definition, as also clear from Fig. 6, values for Λ are such that $0 < \Lambda < 1 (\%v/v)^2$. Clearly values close to the extremes 0 and 1 are only theoretically possible and in reality Λ will tend to converge to values close to the 0.5 uniform distribution.

Figure 7 shows a plot of Λ *vs.* temperature for both unwashed and washed samples.

Values above 200 ℃ (at which we can consider the thermal degradation of the hydrocarbon fraction to begin) are linearly interpolated to calculate the "rate of pore opening towards the center". The data and this interpolation provide two remarkably insightful observations:

1) Pores at the center of a washed sample are opened ~ 3.5 times faster with temperature when compared to unwashed samples;
2) The rate of pore opening towards the center is clearly slower than exponential. As such, this rate does not follow an Arrhenius-like kinetics.

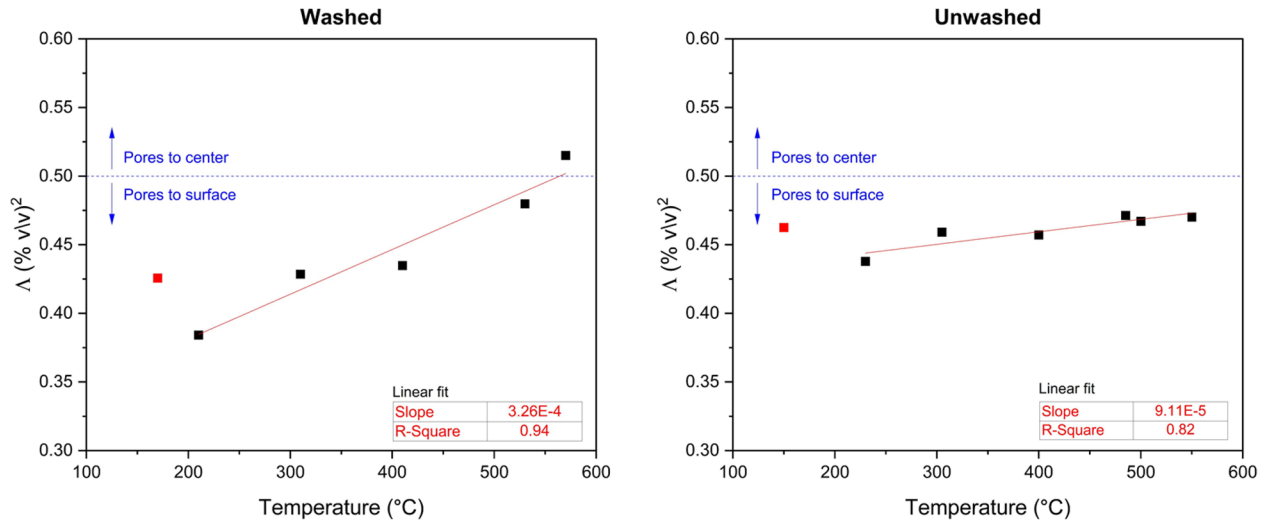

Fig. 7 Normalized cumulative porosity *vs.* normalized distance from surface in unwashed and washed samples. Linear fit is calculated for values from 200 ℃ temperature (black squares). The blue horizontal dashed line at Λ = 0.5 indicates the theoretical condition where the porosity is uniformly distributed throughout particle volume. Values below 0.5 indicate pores distributed more towards the surface, while values above 0.5 indicate pores distributed more towards the center

Point (1) provides additional (and numerical) evidence of the beneficial influence of water pre-washing when the available pore surface is key to a biomass-based application. Point (2) provides a qualitative representation of the influence of (heat and mass) transport limitations on the kinetics of thermochemical decomposition in the temperature range analysed.

3 Discussion

The results in present work allow to synthesise the following significant observations:

1) When heated to 575 ℃ samples of lignified biomass such as WS follow significantly different pathways when pre-washed in deionized water. This is related to the role that aromatics and inorganics play in the thermochemical conversion of biomass. Lignin undergoes a 'softened' phase responsible for an appreciable particle swelling before particle shrinkage occurs from 300 ℃ onward. Lignin is also responsible for a progressive stabilization of particles above that temperature and a significantly lower loss of particle volume compared to a sample in which aromatics and inorganics were partly removed by pre-washing.
2) The loss in particle volume during biomass pyrolysis is linked to numerous chemical reactions occurring in the space of a reactive evolving porous matrix in which the chemical structures of the solid changes due to reactions both in the homogeneous (solid) and heterogeneous (solid–gas solid-vapors) phases. Our results provide clear evidence of the influence that up to approximately 450–500 ℃ the shrinking of particles is related to an evolution of the solid matrix. From that point, the evolving volume appears to be more influenced by the changing pore structure. Differences in the chemical structure of the solid matrix influence heat and mass transport phenomena through the solid, thereby facilitating or slowing some of the reactions' kinetics responsible for the devolatilization process. As such, the present evidence is key to aid existing computational efforts (Everson et al. 2011; Singer and Ghoniem 2011) aimed at resolving the aforementioned chemical reactions undergoing in the evolving porous medium and providing important insights into the influence of particle size, particle shape, and microstructure on observed reaction rates, which are currently lacking (Ciesielski et al. 2020)
3) While a decrease in particle volume occurs via both volatilization of compounds and structural recombination taking place in the solid's phase as temperature rises, porosity also generally tends to increase as volatile compounds escape the solid in the form of vapor or gas. However, owing to the aforementioned transport phenomena, this porosity increases differently with the position inside the particle and again differently if the particle is pre-washed or not. In the latter case the pores in the center of particles increase at a rate ~ 3.5 times faster with temperature to reach values above a uniform distribution of pores across the volume, i.e. a condition where there is more pore area in the center than at the surface.
4) The tracking of pore localization via a purpose-defined parameter Λ with temperature shows a kinetics of pore opening towards the center that is significantly slower than the exponential, thereby showing a visual qualitative observation of the limitation of the chemical reaction kinetics imposed by transport phenomena. The trends shown for Λ provide clues to modelling efforts that attempt at studying the structural evolution of porous biomass particles undergoing thermal treatments in the kinetically limited or pore diffusion-limited regimes such as (Singer and Ghoniem 2011).

It is worth mentioning that the present results are limited to the ~ 0.82 μm resolution of the micro-CT and that a non-negligible influence of the smaller pores would be unveiled from an analysis at the smaller (nanometric) scale. A much more complex and descriptive assessment could be performed by a time/temperature- and space-resolved study of the evolution of the solid's structure (eg. the crystalline *vs.* amorphous nature of carbon in the solid matrix). Multi-scale and multi-analytical *in-situ* techniques should combine nano-CT (for example via ptychography) with other analytical techniques such as *in-situ* x-ray diffraction and x-ray fluorescence, to elucidate the still unresolved role of inorganics during pyrolysis. In addition, the authors believe that significant synergies still remain to be exploited through direct collaborations between modelers at the multiscale level and experimentalists.

4 Conclusions

A method to follow the changes in particle morphology and porosity during biomass pyrolysis via synchrotron-based x-ray computed tomography is presented. Data obtained through a bespoke semi-automated Matlab® image analysis routine showed information of the shrinking particle size with temperature during pyrolysis and the influence of water pre-washing of feedstock. Evidence is presented on the evolution of porosity in particles and its redistribution inside particle volume with temperature. A purpose-defined parameter allowed us to evaluate

the rate at which porosity in the particle 'moves' towards the center which provided important information towards resolving mass- and heat-transport-limited reaction kinetics during biomass pyrolysis at the scale analysed. Overall, our results provide direct observations to aid the numerous computational efforts aimed at resolving the mechanism of biomass thermochemical decomposition towards the tuning of pyrolysis parameters to obtain precision-engineered biochars for environmental applications.

5 Methods

5.1 Materials and sample preparation

Walnut shell (WS) biomass samples sourced from a farm in Sicily (Italy). These shells represent the lignacious endocarp of the fruit, with lignin contents of around 30% w/w. (Queirós et al. 2019) Particles were milled to 2 mm using a Retsch® Ultra Centrifugal Mill, Series ZM 200, 240 V 50/60 Hz and a 2 mm mantle grate. The milled particles were then sieved to obtain 1–2 mm particle sizes in a Retsch® AS 200 Vibratory Sieve Shaker using a 1 mm sieve at an amplitude of 1.7 mm for 6 min. The particles were oven dried at 105 ℃ for 48 h using a Thermo Scientific, Heratherm® oven. Some shells were soaked at a concentration of 50 g L^{-1} in ultrapure deionized (DI) water (electrical conductivity < 1μScm^{-1}) and rinsed through a filter paper before they were again oven dried as described above. All samples were then stored under Ar at − 20 ℃ in order to prevent moisture intake or oxidation.

5.2 Pyrolysis and image acquisition

i) Fixed bed reactor setup

Individual particles of ample were glued using high temperature glue Vitcas® Black Fire Cement 1250 ℃ on a 2 mm dia. ~ 4 cm long quartz rod which was then placed in a 3 mm inner diameter (ID), 4.5 outer diameter (OD), 6 cm long quartz tube which served as a reactor. Aluminum foil was used to fix the sample holding rod to the outer tube. Samples were pre-packed, and the tube ends were sealed using parafilm. Prior to experiments, parafilm was removed and the reactor was placed into a metal holder in turn fixed on an adjustable rotating stage.

The quartz tube was secured in the holder by means of an adjustable side screw to ensure no movement of the reactor as the stage rotated. A resistively heated gas blower, manufactured at Diamond Light Source, was placed close to the quartz tube opening, to blow 10 L min^{-1} hot Ar directly onto the sample, to serve both as heat carrier and sweep gas. The gas blower briefly consisted of a resistively heated tungsten filament of about 1 mm in diameter placed in a quartz tube of about 10 mm in diameter and 20 cm in length, through which the gas was blown. The tungsten filament was heated by means of 220 V 50 Hz current controlled by a power supply by means of a 500 μm dia. K-type thermocouple (TC) placed at the exit of the blower's tube. A feedback loop created between the blower and the power supply controlled by a Proportional Integral Derivative (PID) controller guaranteed a linear temperature increase. The PID program allowed to set input values of the peak temperature (PT), heating rate (HR) and holding time (HT) at PT. Another 500 μm dia. K-type TC was placed inside the sample quartz tube to monitor and register temperature in the sample environment. A less than 50 ℃ temperature difference was recorded between the sample environment and gas blower throughout all experiments. A picture of the set-up is presented in Fig. 8. The position of the heater tube close to the reactor ensured minimal heat loss and importantly, prevented air from entering the reaction zone. A ~ 0.5 cm of tightly packed rock wool was placed inside the bottom end of the quartz reactor to ensure that no air would be dragged in the reactor from its bottom opening.

ii) Pyrolysis reaction

The furnace PID controller was set to ramp 10 K min^{-1} HR to 600 ℃ PT for a 10 min HT at PT. Before starting the heating ramp, the furnace was kept at room temperature for 10 min while 10 L min^{-1} of Ar was blown on the sample to remove any air in the reactor's tube prior to pyrolysis. Once the heater was set to start, we waited for temperature to reach ~ 100 ℃ to start the CT scanning while recording both the furnace and sample temperatures. The latter was recorded as the pyrolysis temperature. The ramps recorded for both unwashed and washed WS are reported in Fig. 9. The average ramps recorded were 12.1 and 12.9 K min^{-1} for the unwashed and washed WS, respectively. The recorded PT was 575 ℃ for both samples.

iii) Optical imaging setup

Experiments were performed at the Diamond-Manchester Imaging Branchline I13-2 (Rau et al. 2011; Rau 2017) of Diamond Light Source (Oxfordshire, UK). A partially coherent, near-parallel, polychromatic 'pink' beam (1.3 mm pyrolytic graphite & 3.2 mm aluminum filters; 8–30 keV; weighted mean ~ 27 keV) was used for the CT imaging. Images were phase-contrast enhanced, with a propagation distance of ~ 50 mm, and collected by a detector (pco.edge 5.5—PCO AG, Germany; sCMOS sensor of 2560 × 2160, 6.5 μm pixels) mounted atop a scintillator-coupled microscope of variable magnification. Magnification was set to give an

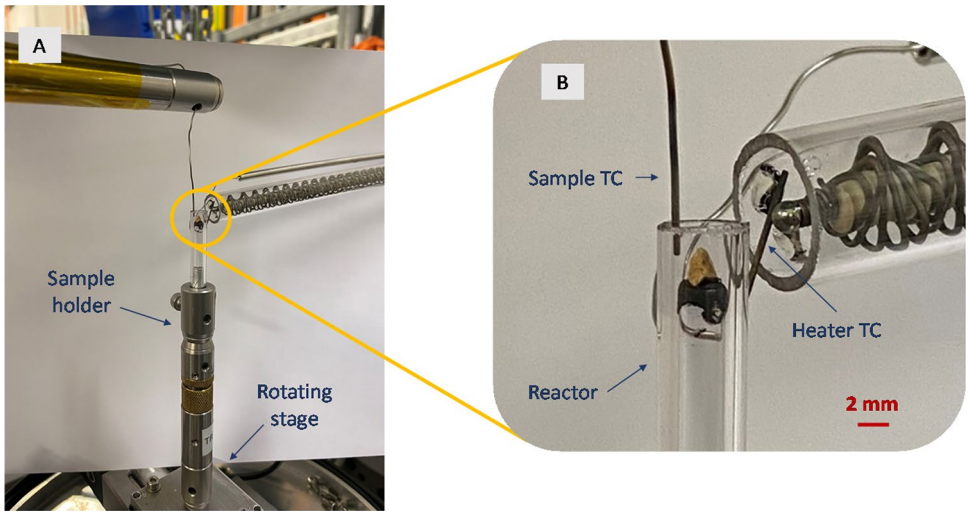

Fig. 8 **A** reactor mounted on rotating stage and (**B**) close-up of the sample environment

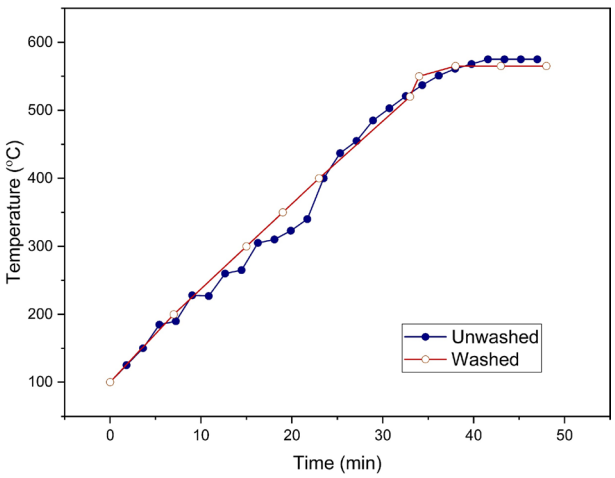

Fig. 9 Pyrolysis temperature ramps for unwashed and washed walnut shells samples

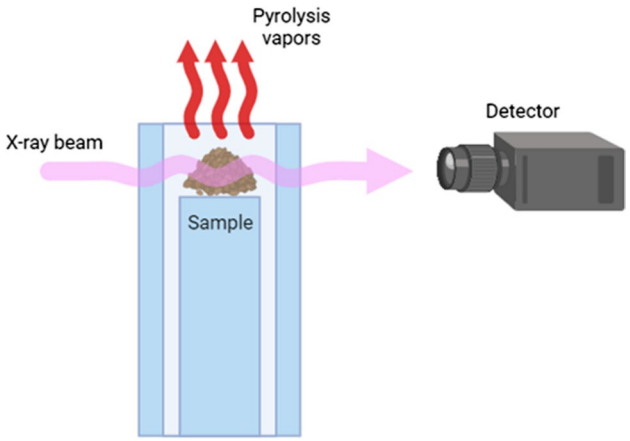

Fig. 10 Schematics of the sample configuration between the x-ray beam source and the detector

effective pixel size of 0.825 µm for data collection, using a 4× magnification, 500 µm LuAG S007 scintillator.

Individual WS particles mounted as showed in Fig. 8 were placed in line with the x-ray beam and the detector as schematized in Fig. 10. A series of 63 scans were acquired for each pyrolysis run at equally spaced angles over 180° of continuous rotation ('fly scan'), with an extra projection (not used for reconstructions) collected at 180° to check for sample deformation and bulk movements relative to the first (0°) projection (Atwood et al. 2015). The following 2 scanning conditions were applied. Condition 1 consisted of 1,800 projections acquired with an integration time of 0.1 s per frame. This was used for both the initial (or reference) scan, corresponding to the sample at room temperature before pyrolysis, labelled as "raw", and the final scan after pyrolysis, again at room temperature, labelled as "char" (for biochar). Condition 2 consisted of 1,800 scans and an integration time of 0.005 s, for the ramp up to the PT.

Longer exposure times allowed for a better image contrast for the CT scans of the 'static' raw and char samples. The shorter exposure time meant each CT scan during pyrolysis required approximately 90 s. This time was chosen as a good compromise between obtaining sufficient contrast images and reducing the heat gradient (and sample changes in morphology) between the first and last projection of each *operando* scan.

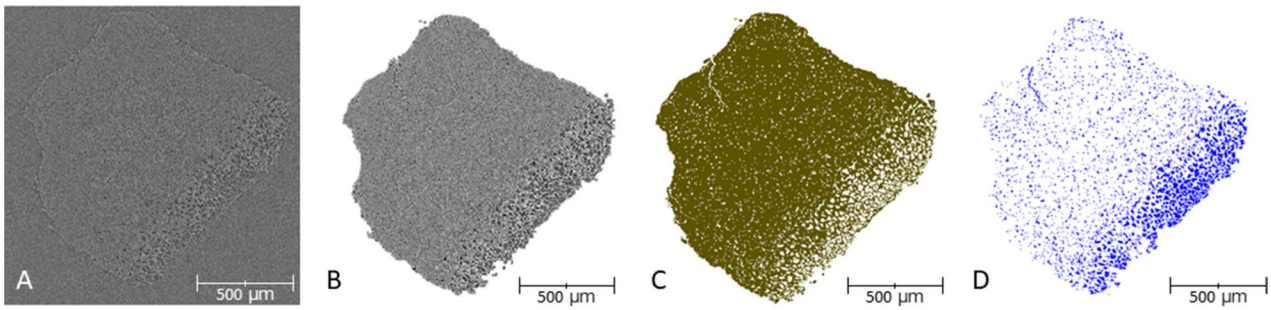

Fig. 11 Schematic representation of the main steps carried out for the image processing methodology developed applied to washed walnut shell scan. **A** Original image, **B** Image filtered and segmented from the background, **C** Binary image corresponding to particle material, **D** Binary image corresponding to pores

5.3 Image processing methodology

An automated image processing methodology based on a series of Matlab® and Avizo® routines was developed with the main aim of producing statistically meaningful, reproducible results. This methodology comprises a preliminary cleaning stage to improve image quality due to the low signal-to-noise ratio of the acquired images. The cleaned images were segmented into three phases, namely: pores, particle material, and background.

Obtaining the binary masks for each scanning point was challenging due to the significant variations on image contrast throughout the process. The combination of mass loss and change in size of the WS caused the image histograms to vary widely, and it was not possible to use a single image processing routine for all scans in the data set (i.e. the masks could not be generated by batch processing). Alternatively, a step-by-step approach was used to assess the best segmentation methods for each stage. In the first instance, and with the aim of minimising computational resources and to optimise the image processing analysis, only 1 scan every 10 was used to assess the best methodology for different points in the data set. These scans were selected so that they represent different stages in the process.

Once the segmentation routines were determined for the different stages (i.e. different temperatures), the two sets of 63 scans were segmented and the morphological changes were quantified by tracking the changes of the mask and not the original images to avoid introducing errors associated with the measured volume. Such error is mitigated by projecting a mask onto the appropriate grid in order to identify the relevant morphological changes on the original untransformed image. This permitted to produce a 4D quantification library.

The main processing steps (Fig. 11) can be described as follows:

1. Noise was reduced by using different global filtering methods. The best results were obtained by using median filters at low temperatures, and Gaussian filters at higher temperatures.
2. A combination of watershed segmentation methods, careful thresholding, and morphological operations, such as opening and closing, were performed to segment the particle and its internal pores from the background. A binary mask was produced for the binarized image.
3. A normalized distance map was produced for each time step by dividing each distance value by the maximum distance to the surface. The main reason for this was to take into consideration the expansion/contraction taking place at each stage of the process, so the porosity profile can be compared at different stages of the process.
4. The pore network was analysed at different locations of the sample using the normalised distance map produced in step 3.

This method is novel and opens the way to a fully automated procedure for the analysis of complex data such as those represented in the present work.

Acknowledgements

This research was supported by Queen Mary University of London. We acknowledge Diamond Light Source for time on beamline I13 under Proposal MG25254. The authors would like to gratefully thank Dr Sylvia Britto and Dr Konstantin Ignatyev of DLS I18 beamline for the kind support with the furnace. The authors would also like to extend their very special thanks to Dr Kaz Wanelik for the invaluable, tireless support with the software management during experiments and data retrieval during preparation of this manuscript.

Author contributions

L.S.F wrote the analysis codes; reconstructed and segmented tomograms; prepared the images; organized data and contributed to their analysis; contributed to preparation of the manuscript. M.C.M prepared the biomass and the samples' reactor; operated the furnace during experiments; contributed to preparation of the manuscript; R.J. contributed to data processing, and contributed expertise; contributed to editing the manuscript; S.M. operated the imaging equipment; C.R. contributed use of the I13 Branchline facilities and

expertise; R.V. conceived the study, obtained the biomass, contributed to reactor design, operated the reactor, and contributed supervision and expertise. All authors have reviewed the contents of the manuscript.

Data availability

The authors declare that the codes used to clean and segment images for the analysis in this study are available within the paper and its Supplementary material. Should any raw data files be needed in another format they are available from the corresponding author upon reasonable request.

Declarations

Competing interests

The authors declare no competing interests.

Author details

[1]School of Engineering and Materials Science, Queen Mary University of London, London E1 4NS, UK. [2]Department of Earth Science and Engineering, Imperial College London, London SW7 2AZ, UK. [3]Department of Chemical Engineering, University College London, Gower Street, London WC1E 7JE, UK. [4]Diamond Light Source, Harwell Science & Innovation Campus, Didcot OX11 0DE, UK.

Received: 18 March 2024 Revised: 22 July 2024 Accepted: 30 July 2024
Published online: 11 October 2024

References

Antal MJ, Grønli M (2003) The art, science, and technology of charcoal production †. Ind Eng Chem Res 42:1619–1640. https://doi.org/10.1021/ie020 7919

Atwood RC, Bodey AJ, Price SWT et al (2015) A high-throughput system for high-quality tomographic reconstruction of large datasets at diamond light source. Philos Trans A Math Phys Eng Sci. https://doi.org/10.1098/rsta.2014.0398

Barr M, Volpe R (2021) Kandiyoti R Identifying synergistic effects between biomass components during pyrolysis and pointers concerning experiment design. ACS Sustain Chem Eng 9:5603–5612. https://doi.org/10.1021/acssuschemeng.1c00051

Barr MR, Volpe R, Kandiyoti R (2019) Influence of reactor design on product distributions from biomass pyrolysis. ACS Sustain Chem Eng. https://doi.org/10.1021/acssuschemeng.9b01368

Barr MR, Volpe M, Messineo A, Volpe R (2020) On the suitability of thermogravimetric balances for the study of biomass pyrolysis. Fuel. https://doi.org/10.1016/j.fuel.2020.118069

Barr MR, Jervis R, Zhang Y et al (2021) Towards a mechanistic understanding of particle shrinkage during biomass pyrolysis via synchrotron X-ray microtomography and in-situ radiography. Sci Rep. https://doi.org/10.1038/s41598-020-80228-x

Barr MR, Forster L, D'Agostino C, Volpe R (2022) Alkaline pretreatment of walnut shells increases pore surface hydrophilicity of derived biochars. Appl Surf Sci 571:151253. https://doi.org/10.1016/j.apsusc.2021.151253

Bates RB, Ghoniem AF (2012) Biomass torrefaction: modeling of volatile and solid product evolution kinetics. Bioresour Technol 124:460–469. https://doi.org/10.1016/j.biortech.2012.07.018

Bates RB, Altantzis C, Ghoniem AF (2016) Modeling of biomass char gasification, combustion, and attrition kinetics in fluidized beds. Energy Fuels 30:360–376. https://doi.org/10.1021/acs.energyfuels.5b02120

Cho Y, Kong S-C (2023) Modeling biomass particle evolution at pyrolysis conditions considering shrinkage and chemical kinetics with conjugate heat transfer. Energy Fuels 37:5926–5941. https://doi.org/10.1021/acs.energyfuels.2c03892

Ciesielski PN, Pecha MB, Lattanzi AM et al (2020) Advances in multiscale modeling of lignocellulosic biomass. ACS Sustain Chem Eng 8:3512–3531

Dadi VS, Veluru S, Tanneru HK et al (2023) Recent advancements of CFD and heat transfer studies in pyrolysis: a review. J Anal Appl Pyrolysis. https://doi.org/10.1016/j.jaap.2023.106163

Deng L, Long J, Wu Y, Che D (2020) A study on benzene release during water washing of biomass. Asia-Pacific J Chem Eng. https://doi.org/10.1002/apj.2536

Di Blasi C (1997) Influences of physical properties on biomass devolatilization characteristics. Fuel 76:957–964. https://doi.org/10.1016/S0016-2361(97)00096-3

Di Blasi C (2008) Modeling chemical and physical processes of wood and biomass pyrolysis. Prog Energy Combust Sci 34:47–90. https://doi.org/10.1016/j.pecs.2006.12.001

Eriksson I, Haglind I, Lidbrandt O, Sahnén L (1991) Fiber swelling favoured by lignin softening. Wood Sci Technol 25:135–144. https://doi.org/10.1007/BF00226813

Everson RC, Neomagus HWJP, Kaitano R (2011) The random pore model with intraparticle diffusion for the description of combustion of char particles derived from mineral- and inertinite rich coal. Fuel 90:2347–2352. https://doi.org/10.1016/j.fuel.2011.03.012

Guo X, Gao G, Remón J et al (2022) Selective hydrogenation of vanillin to vanillyl alcohol over Pd, Pt, and Au catalysts supported on an advanced nitrogen-containing carbon material produced from food waste. Chem Eng J. https://doi.org/10.1016/j.cej.2022.135885

Hu B, Zhang B, Xie W-L et al (2020) Recent progress in quantum chemistry modeling on the pyrolysis mechanisms of lignocellulosic biomass. Energy Fuels 34:10384–10440. https://doi.org/10.1021/acs.energyfuels.0c01948

Janse AMC, Westerhout RWJ, Prins W (2000) Modelling of flash pyrolysis of a single wood particle. Chem Eng Process 39:239–252. https://doi.org/10.1016/S0255-2701(99)00092-6

Kandiyoti R, Herod AA, Bartle KD, Morgan TJ (2017) Solid fuels and heavy hydrocarbon liquids, thermal characterisation and analysis, 2nd edn. Elsevier Science Publishers, Amsterdam

Klose W, Schinkel A (2002) Measurement and modelling of the development of pore size distribution of wood during pyrolysis. Fuel Process Technol 77–78:459–466. https://doi.org/10.1016/S0378-3820(02)00082-6

Krasucka P, Pan B, Sik Ok Y et al (2021) Engineered biochar—A sustainable solution for the removal of antibiotics from water. Chem Eng J 405:126926

Lee K, Roy S, Cakmak E et al (2020) Composition-preserving extraction and characterization of biomass extrinsic and intrinsic inorganic compounds. ACS Sustain Chem Eng 8:1599–1610. https://doi.org/10.1021/acssuschemeng.9b06429

Li J, Campos LC, Zhang L, Xie W (2022) Sand and sand-GAC filtration technologies in removing PPCPs: a review. Sci Total Environ 848:157680. https://doi.org/10.1016/j.scitotenv.2022.157680

Li X, Cao H, Cao Y et al (2023) Insights into the mechanism of persulfate activation with biochar composite loaded with Fe for 2,4-dinitrotoluene degradation. J Environ Manage. https://doi.org/10.1016/j.jenvman.2023.117955

Liu WJ, Jiang H, Yu HQ (2015) Development of biochar-based functional materials: toward a sustainable platform carbon material. Chem Rev 115:12251–12285. https://doi.org/10.1021/acs.chemrev.5b00195

Lorenz K, Lal R (2014) Biochar application to soil for climate change mitigation by soil organic carbon sequestration. J Plant Nutr Soil Sci 177:651–670. https://doi.org/10.1002/jpln.201400058

Malik W, Victoria Tafoya JP, Doszczeczko S et al (2023) Synthesis of a graphene-encapsulated Fe_3 C/Fe catalyst supported on sporopollenin exine capsules and its use for the reverse water-gas shift reaction. ACS Sustain Chem Eng. https://doi.org/10.1021/acssuschemeng.3c00495

Mettler MS, Vlachos DG, Dauenhauer PJ (2012) Top ten fundamental challenges of biomass pyrolysis for biofuels. Energy Environ Sci 5:7797. https://doi.org/10.1039/c2ee21679e

Mohanty SK, Boehm AB (2015) Effect of weathering on mobilization of biochar particles and bacterial removal in a stormwater biofilter. Water Res 85:208–215. https://doi.org/10.1016/j.watres.2015.08.026

Mohanty SK, Cantrell KB, Nelson KL, Boehm AB (2014) Efficacy of biochar to remove *Escherichia coli* from stormwater under steady and intermittent flow. Water Res 61:288–296. https://doi.org/10.1016/j.watres.2014.05.026

Morgan TJ, Kandiyoti R (2014) Pyrolysis of coals and biomass: analysis of thermal breakdown and its products. Chem Rev 114:1547–1607. https://doi.org/10.1021/cr400194p

Mosonik MC, Volpe R, Ezenwajiaku C et al (2021) In situ observation of the evolution of polyaromatic tar precursors in packed-bed biomass pyrolysis. React Chem Eng 6:1538–1547. https://doi.org/10.1039/d1re00032b

Queirós CSGP, Cardoso S, Lourenço A et al (2019) Characterization of walnut, almond, and pine nut shells regarding chemical composition and extract composition. Biomass Convers Biorefin 10:175–188. https://doi.org/10.1007/s13399-019-00424-2

Rau C (2017) Imaging with coherent synchrotron radiation: X-ray imaging and coherence beamline (I13) at diamond light source. Synchrotron Radiat News 30:19–25. https://doi.org/10.1080/08940886.2017.1364530

Rau C, Wagner U, Pešić Z, De Fanis A (2011) Coherent imaging at the diamond beamline I13. Phys Status Solidi (a) 208:2522–2525. https://doi.org/10.1002/pssa.201184272

Rodriguez Correa C, Hehr T, Voglhuber-Slavinsky A et al (2019) Pyrolysis vs. hydrothermal carbonization: understanding the effect of biomass structural components and inorganic compounds on the char properties. J Anal Appl Pyrolysis 140:137–147. https://doi.org/10.1016/J.JAAP.2019.03.007

Shafawi AN, Mohamed AR, Lahijani P, Mohammadi M (2021) Recent advances in developing engineered biochar for CO2 capture: an insight into the biochar modification approaches. J Environ Chem Eng. https://doi.org/10.1016/j.jece.2021.106869

Singer SL, Ghoniem AF (2011) An adaptive random pore model for multimodal pore structure evolution with application to char gasification. Energy Fuels 25:1423–1437. https://doi.org/10.1021/ef101532u

Singer SL, Ghoniem AF (2013) Comprehensive gasification modeling of char particles with multi-modal pore structures. Combust Flame 160:120–137. https://doi.org/10.1016/j.combustflame.2012.09.007

Singh T, Arpanaei A, Elustondo D et al (2022) Emerging technologies for the development of wood products towards extended carbon storage and CO2 capture. Carbon Capture Sci Technol 4:100057

Stiles H, Kandiyoti R (1989) Secondary reactions of flash pyrolysis tars measured in a fluidized bed pyrolysis reactor with some novel design features. Fuel 68:275–282

Tagar U, Volpe M, Messineo A, Volpe R (2023) Highly ordered CaO from cuttlefish bone calcination for the efficient adsorption of methylene blue from water. Front Chem 11:1132464. https://doi.org/10.3389/FCHEM.2023.1132464/BIBTEX

Taylor MJ, Alabdrabalameer HA, Michopoulos AK et al (2020) Augmented leaching pretreatments for forest wood waste and their effect on ash composition and the lignocellulosic network. ACS Sustain Chem Eng 8:5674–5682. https://doi.org/10.1021/acssuschemeng.0c00351

Uday V, Harikrishnan PS, Deoli K et al (2022) Current trends in production, morphology, and real-world environmental applications of biochar for the promotion of sustainability. Bioresour Technol 359:127467. https://doi.org/10.1016/J.BIORTECH.2022.127467

Volpe R, Messineo A, Millan M et al (2015) Assessment of olive wastes as energy source: pyrolysis, torrefaction and the key role of H loss in thermal breakdown. Energy 82:119–127. https://doi.org/10.1016/j.energy.2015.01.011

Volpe R, Messineo A, Millan M (2016) Carbon reactivity in biomass thermal breakdown. Fuel 183:139–144. https://doi.org/10.1016/j.fuel.2016.06.044

Volpe R, Zabaniotou A, Skoulou V (2018) Synergistic effects between lignin and cellulose during pyrolysis of agricultural waste. Energy Fuels 32:8420–8430. https://doi.org/10.1021/acs.energyfuels.8b00767

Volpe R, Bermudez Menendez JM, Ramirez Reina T et al (2019a) Free radicals formation on thermally decomposed biomass. Fuel. https://doi.org/10.1016/j.fuel.2019.115802

Volpe R, Bermudez Menendez JM, Ramirez Reina T et al (2019b) Free radicals formation on thermally decomposed biomass. Fuel 255:115802. https://doi.org/10.1016/J.FUEL.2019.115802

Yang L, Liang C, Shen F et al (2023) A critical review on the development of lanthanum-engineered biochar for environmental applications. J Environ Manage. https://doi.org/10.1016/j.jenvman.2023.117318

Younis SA, Kim K-H (2022) Recent Advances in biochar-based catalysts: air purification and opportunities for industrial upscaling. Asian J Atmos Environ. https://doi.org/10.5572/ajae.2022.117